Investigation of the Avalanche Fluctuations Factor in a Time Projection Chamber Detector Using 266 nm UV Laser*

Yue Chang,[1,2] Hui-Rong Qi,[2,3] Xin She,[2,3] Jin-Xian Zhang,[2,3] Guang Zhao,[2,3] Hong-Liang Dai,[2,3] Chun-Xu Yu,[1] Ling-Hui Wu,[2,3] Zhi Deng,[4] Yi-Fang Wang,[2] Jian-Chun Wang,[2,3] Yuan-Bo Chen,[2] and Jian Zhang[2]

[1]*School of Physics, Nankai University, Tianjin 300071, China*
[2]*State Key Laboratory of Particle Detection and Electronics (Institute of High Energy Physics, CAS), Beijing 100049, China*
[3]*University of Chinese Academy of Sciences, Beijing 100049, China*
[4]*Department of Engineering Physics, Tsinghua University, Beijing 100084, China*

Time Projection Chambers (TPCs) are extensively used in collider experiments due to their superior physical performance. Particularly for future positron-electron colliders in Higgs physics studies, the next-generation TPC technology must provide better momentum resolution and improved spatial resolution. The avalanche fluctuation factor, a crucial parameter affecting spatial resolution, is challenging to measure accurately, whether directly or indirectly. This research leveraged the exceptional stability and ionization properties of ultraviolet (UV) lasers to achieve a precise determination of the avalanche fluctuation factor. The test outcomes were found to agree with the calculated values at the same gain levels, thereby validating the reliability of the experimental findings.

Keywords: Time Projection Chamber, UV laser, Avalanche fluctuation, Gas gain

I. INTRODUCTION

The Time Projection Chamber (TPC) [1] is a tracking detector renowned for its high-precision measurements of particle momentum, position and ionization energy loss, which are crucial for accurate particle identification. In addition, the TPC is characterized by low material budget and excellent pattern recognition capabilities. Its capabilities have made the TPC a staple in particle physics experiments, as well as in low-energy nuclear physics and the study of double beta decay [2–4]. The TPC has recently been confirmed as the baseline main tracker detector in the Circular Electron Positron Collider Reference Technical Design Report (CEPC refTDR) [5, 6]. Moreover, the International Linear Collider (ILC) [7] also intends to adopt the TPC as its track detector.

In particular, for Higgs physics research in future positron-electron colliders [8], the accuracy of the measurements is heavily dependent on the position resolution of the TPC σ_x, which underscores the importance of measuring and optimizing the parameters that affect this resolution. To meet the demands for precise measurements of Higgs properties, the next-generation TPC aims to achieve a position resolution of approximately 100 μm for tracks that are meters in length. The parameters affecting σ_x are detailed in Eq. (1) [9, 10]:

$$\sigma_x^2 = \sigma_0^2 + \frac{D_T^2}{N_{eff}} z + \frac{h^2}{12N_{eff}} \tan^2\phi \tag{1}$$

The term σ_0 represents the influence of factors such as electronic noise and electron amplification fluctuations on the resolution. The second term accounts for the influence of drift and diffusion on position resolution, which is a primary determinant of the overall resolution. Here, D_T signifies the electron diffusion coefficient, N_{eff} represents the effective number of electrons, z is the drift distance, and h refers to the shorter width of the pad readout electrode. Since electrons are generated in clusters, the relevant measurement for particle detection is the N_{eff} over a specific length of the readout pad in the end plate, rather than the total number of electrons along the track segment. The third term considers the effects of track angles ϕ with respect to the pad row, pad size and N_{eff} on position resolution. The N_{eff} is defined as [11, 12]:

$$\frac{1}{N_{eff}} = (1+f)\langle\frac{1}{n}\rangle \tag{2}$$

n is the number of primary ionization electrons reaching the sensitive area covered by the pad row and $f = \sigma_G^2/\langle G\rangle^2$(where G is the gas gain and σ_G is the standard deviation of gain) denotes the avalanche fluctuations factor. Ideally, we expect that N_{eff} would match the average number of ionization electrons $\langle N\rangle$, in which case $f = 0$. However, in reality, N_{eff} is reduced by avalanche fluctuations and is commonly found to be only 30% $\sim$ 40% of $\langle N\rangle$ [13]. As the factor f increases, it indicates that the uncertainty in gain also rises, thereby affecting the position resolution of the detector.

Position resolution is affected by various parameters, making it a key component in the design and optimization of TPCs [9]. The uncertainties associated with the parameters in Eq. (1) can be reduced via dedicated measurements using Micro Pattern Gas Detectors (MPGD), such as GEM [14, 15] and Micromegas [16, 17]. For the CEPC-TPC design, the T2K gas mixture (Ar:CF_4:iC_4H_{10} = 95:3:2) has been selected as the working gas. This mixture has a lower diffusion coefficient, D_T, of approximately 43 $\mu m/\sqrt{\text{cm}}$ compared to other mixtures, under the conditions of a 2 T magnetic field and an electric field strength of 200 V/cm. This characteristic allows for acceptable resolution degradation even at the max-

* Supported by the National Natural Science Foundation of China (Grant No.11975256, No.11775242 and No.12475200) and the National Key Research and Development Program of China (No. 2016YFA0400400)

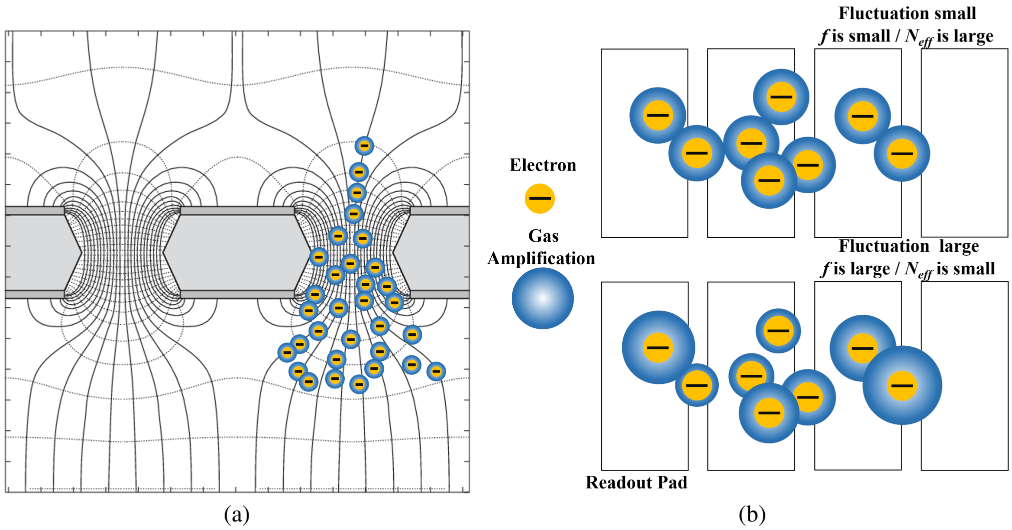

Fig. 1. (a) Schematic diagram of the electric field structure and amplification at the micro-pores of the GEM; (b) The charge distribution on the readout pad of the GEM with the avalanche fluctuation factor f: the upper image represents a schematic diagram for a smaller f, whereas the lower image depicts the outcome for a larger f.

imum drift distance of 290 cm, which is half the length of the CEPC-TPC. However, precisely determining the critical parameter $Neff$ during the initial stages of detector design is challenging, primarily due to the difficulty in accurately measuring the crucial avalanche fluctuations factor, f, either directly or indirectly.

In GEM detectors, the factor f represents the gain uncertainty due to fluctuations near the micropores, as shown in Fig. 1(a). A more stable gain corresponds to a lower f value, which ensures that the induced charge on each pad accurately reflects the distribution of primary ionization. This accuracy enables precise positional information to be obtained through the center-of-gravity method, which calculates the position of a detected ionization event by taking the weighted average of the charge distribution. Conversely, as illustrated in the lower section of Fig. 1(b), an increase in gain uncertainty leads to a significant deviation of the charge distribution on each pad from the primary ionization, resulting in a higher f value and reduced accuracy of position information. Consequently, accurately determining the avalanche fluctuations factor f is crucial for establishing the detector's operating conditions, such as gas type and pressure, as well as for optimizing its performance and enhancing overall precision.

Experimental studies often involve analyzing the gas amplification charge spectrum generated by a single photoelectron from cathode materials. This process is typically facilitated by illuminating materials with LED lamps or lasers to assess avalanche fluctuations. The CERN-RD51 research group directly measured the factor f based on the single-electron response (SER) of a Micromegas detector, achieving a value of $f \sim 0.6$ in a gas mixture of (Ar:iC_4H_{10} = 95:5) [18]. This method is, however, not easy because of electronic noise interference, especially for low gas gains. Concurrently, the PandaX collaboration is exploring the factor f utilizing a liquid Xenon TPC [19, 20].

The factor f can be estimated through Monte Carlo simulations. We used COMSOL Multiphysics simulation software [21] to model the smallest periodic unit of a standard CERN GEM [14], which has a hole diameter of 70 μm and a pitch of 140 μm. The thickness of the upper and lower copper layers is 5 μm, and the Kapton foil is 50 μm thick. After modeling, we imported the resulting mesh and field files into Garfield++ [22] for detailed simulation. The simulation employed a triple-GEM structure, with a 1 mm gap between the GEM foils forming the transfer region, and a 2.5 mm gap between the GEM foil and the readout pad forming the induction region. The simulation was conducted in T2K gas (Ar: CF_4: iC_4H_{10} = 95:3:2). Schematic diagrams of the simulation process and the structure of the GEM unit are shown in Fig. 2 (a). The gas gain (G) simulation results were fitted using a so-called Pólya distribution [23] , as shown in the Fig. 2 (b). The Pólya distribution ($P(G)$) is expressed as Eq. (3):

$$P(G) = C_0 \frac{(1+\theta)^{(1+\theta)}}{\Gamma(1+\theta)} \left(\frac{G}{\langle G\rangle}\right)^{\theta} exp\left[-(1+\theta)\frac{G}{\langle G\rangle}\right] \quad (3)$$

where C_0 is a constant, $\langle G\rangle$ represents the mean gain of the single-electron amplification distribution, and θ is a free parameter determining the shape of distribution. The avalanche fluctuation factor f can be defined as [12]:

$$f = \frac{1}{1+\theta} \quad (4)$$

By fitting the results with Eq. (3), we obtained the values for C_0, $\langle G\rangle$, and θ, leading to an estimation of the factor f, using Eq. (4). The simulations indicate that the value of f is approximately 0.66 with a gain of 1089 in T2K gas.

In recent years, our research has concentrated on experiments involving a 266 nm UV laser [24–28]. We have used its ionization properties to assess the factor f. This method leverages the ionization tracks produced by the UV laser, providing a direct testing approach that minimizes data acquisi-

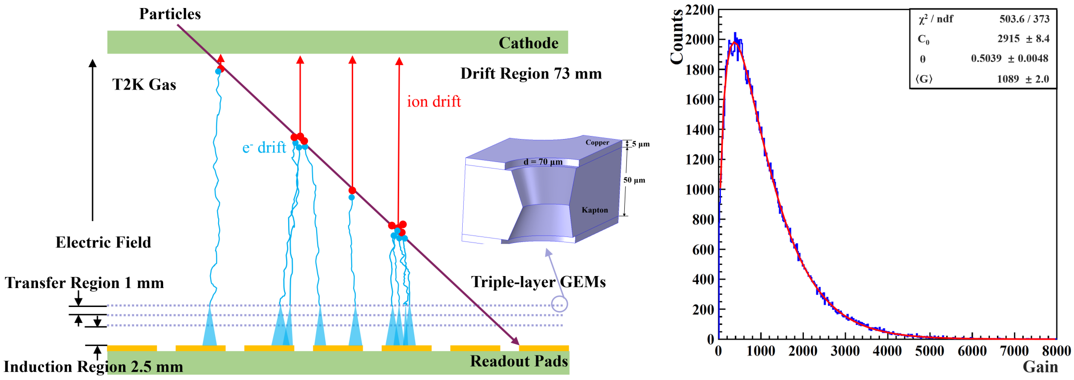

(a) (b)

Fig. 2. (a) Schematic diagram of the simulation process and the smallest periodic unit of a standard GEM; (b) The simulation results of the triple-layer GEMs with fitting using Pólya distribution.

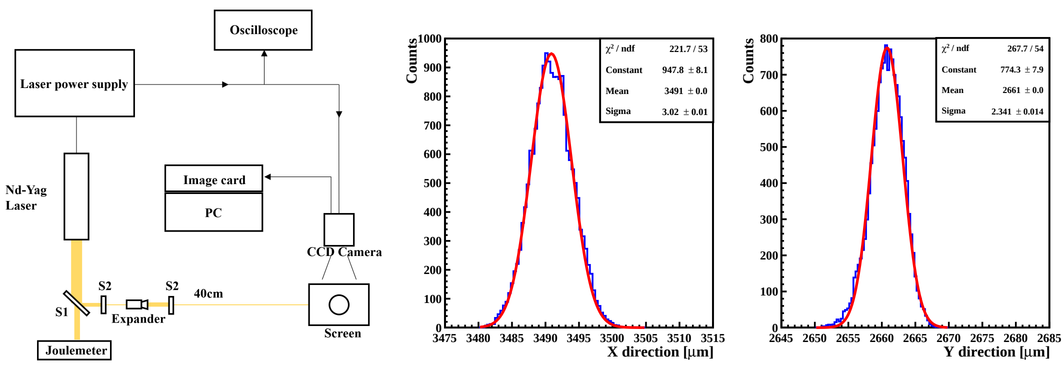

(a) (b)

Fig. 3. (a) The layout of the laser point stability experiment; (b) The fluctuation of the beam spot projected along the X-direction and Y-direction.

tion times. Furthermore, the laser's exceptional monochromaticity and high stability contribute to the uniformity of ionization clusters along the tracks, thereby enhancing the precision of f measurements. The purpose of this paper is to describe the principles and setup of our testing methodology and to present the measured values for the factor f.

II. STABILITY TESTING AND PRINCIPLES OF UV LASER OPERATION

A. Laser Ionization Mechanisms and Laser Selection

The ionization potentials of gases frequently employed in TPCs, such as argon (Ar, 15.7 eV), isobutane (iC_4H_{10} 10.78 eV), methane (CH_4, 13.1 eV), tetrafluoromethane (CF_4, 16.8 eV) [9], are considerably higher than the photon energies of UV lasers. Consequently, these lasers cannot ionize the working gas through the photoelectric effect. For example, the photon energy emitted by an N_2 laser with a wavelength of 377 nm is approximately 3.68 eV, while that from a Nd-YAG laser with a wavelength of 266 nm is about 4.68 eV. However, research by Towrie et al. [29] has established that UV lasers can induce ionization of organic impurity gases present in the working gas. These impurities, with their complex energy level structures, primarily undergo two-photon ionization when interacting with UV lasers [30]. Consequently, advanced laser systems have been developed in STAR-TPC [31] and ALICE-TPC [32] to measure and monitor detector performance by creating uniformly distributed laser tracks throughout the detector system [33].

In our experiment, we utilized the Q-smart 100 Nd-YAG laser by Quantel [34], operating at a wavelength of 266 nm. The laser beam features a diameter of 5 mm and a divergence of approximately 0.3 mrad. The energy of the laser is adjustable, with a maximum output of 20 mJ, and its frequency can be tuned up to 20 Hz. In our previous research, we discovered a power-law relationship between laser ionization density and energy density [26]. Additionally, for TPCs studies, the ionization density of the laser should correspond to 1∼2 minimum ionizing particles (MIPs), equating to 100 to 200 primary ionization electrons per centimeter. This is realized when the laser is operated with an energy density of 1∼2 $\mu J/mm^2$ [26, 31].

B. UV Laser Alignment Stability Testing

Temperature variations and vibrations can interfere with beam alignment, resulting in drift or jitter. Therefore, conducting quantitative tests to assess the stability of laser beam alignment is crucial. This stability is evaluated using a CCD camera, as shown in Fig. 3(a). The laser beam is first directed through a (99/1) partially reflective mirror (S1), which reduces the laser's energy. Only 1% of the laser pulse energy passes through S1, while the rest is measured by a Joulemeter monitor (StarLite from Ophir Corp. [35]). Then, two diaphragms (S2) are used to collimate the beam and further narrow the spot diameter to 0.8 mm. A 3X beam expander, which increases the spot diameter of the Gaussian laser beam to 2.4 mm, is placed between the diaphragms. The second diaphragm helps select a laser beam with a more uniform energy distribution. The diaphragm-expander-diaphragm configuration further reduces the pulse energy.

The spot center fluctuation is represented by two Gaussian functions in the X and Y direction, as shown in Fig. 3(b), with standard deviations of about 3.02 μm in the X direction and 2.34 μm in the Y direction. This high stability level ensures precise measurement of the avalanche fluctuation factor.

C. UV Laser Energy Stability Testing

In practical applications, variations in the total energy output of laser systems are unavoidable, primarily due to temperature fluctuations that affect crystal performance and the inherent variations in emitted radiative photons during laser operation. For Nd-YAG lasers that utilize frequency-doubling, temperature changes within the system can particularly impact the performance of the frequency-doubling crystal. Although the laser's internal cooling system can partially offset these effects, it is crucial to test the stability of the laser energy to ensure accurate assessments.

To satisfy the experimental demands for microjoule-level laser energy, the energy stability of the attenuated narrow-beam laser was tested using the Ophir energy monitoring system. The testing period lasted 20 minutes, with the results presented in Fig. 4. The test results indicate that the average energy of the low-energy laser after attenuation is 46.59 μJ, with energy stability better than 2.9%. This degree of energy stability meets the requirements for measuring the gain stability factor.

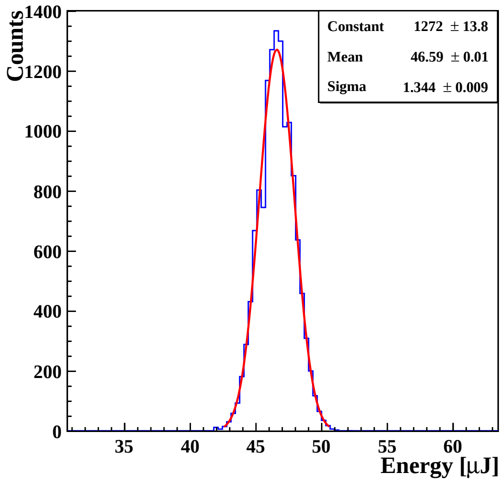

Fig. 4. The results of the UV laser's energy stability during a 20-minute testing duration.

III. AVALANCHE FLUCTUATIONS FACTOR TESTING

A. Measurement Principle

As mentioned in Eq. (2), the effective number of electrons, denoted as N_{eff} depends on the factor f and the number of average primary ionization electrons on pad row, $\langle n \rangle$. The laser's precise monochromaticity and stability are instrumental in ensuring consistent ionization cluster sizes. Consequently, with a stable primary ionization, N_{eff} is primarily determined by the factor f. Moreover, the laser beam energy density can be adjusted to achieve an ionization rate equivalent to 1$\sim$2 MIPs.

Recent studies have demonstrated that the laser ionization energy spectrum adheres to a Gaussian distribution after calibration, aligning with the energy distribution of the laser beam itself. The factor f can be determined by comparing the charge signals Q_1 and Q_2, which are collected by adjacent pad rows after the ionized electrons produced by the laser beam have been amplified. The theoretical underpinnings of this method are derived from the literature [36, 37].

The total number of amplified electrons, N, collected by a pad row can be represented by Eq. (5):

$$N = \sum_{i=1}^{n} g_i = g_1 + g_2 + \cdots + g_n \tag{5}$$

where N is the total number of primary electrons generated within a pad row's range by laser ionization. g_i is the avalanche size of the i-th electron. The average number and variance of amplified electrons are expressed in Eqs. (6) $\sim$ (8):

$$\langle N \rangle = \langle n \rangle \cdot \langle g \rangle \tag{6}$$

Then, the average of $\langle N \rangle$, $\langle\langle N \rangle\rangle$ is defined by:

$$\langle\langle N \rangle\rangle = \langle\langle n \rangle\rangle \cdot \langle g \rangle \tag{7}$$

$$\begin{aligned} \sigma_N^2 &\equiv \left\langle (N - \langle N \rangle)^2 \right\rangle \\ &= \langle n \rangle \cdot \langle g \rangle^2 \cdot \left(\frac{\sigma_n^2}{\langle n \rangle} + f\right) \end{aligned} \tag{8}$$

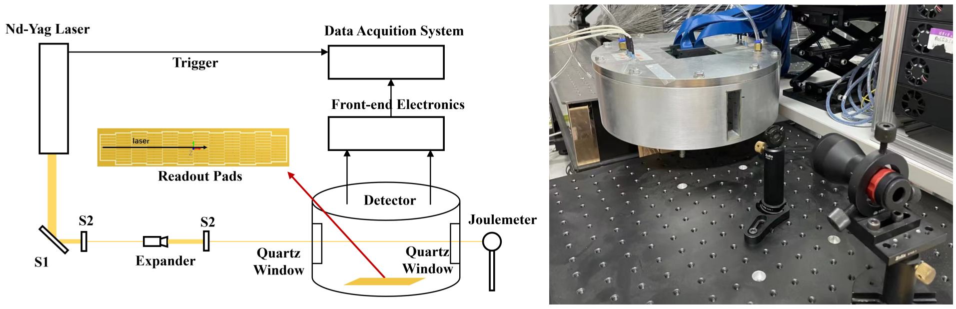

(a) (b)

Fig. 5. (a) Layout of the experimental device; (b) The photo of the detector chamber.

The fluctuation in primary ionization is indicated by $\sigma_n^2/\langle n\rangle$ with $\langle n\rangle$ being the average number of primary electrons per laser shot on a pad row. While the notation $\langle\langle n\rangle\rangle$ represents the average of $\langle n\rangle$ for all laser shots over the entire experimental period. The average number of amplified electrons collected by a single readout pad row during a single laser pulse is represented by $\langle N\rangle = \langle g\rangle \cdot \langle n\rangle$, with $\langle g\rangle$ being the gain of electrons.

Then, the factor f can be obtained by calculating the variance of the number of amplified electrons collected by two nearby pad rows during a single experimental measurement as Eq. (9):

$$\begin{aligned}\left\langle (N_1 - N_2)^2 \right\rangle &= \left\langle ((N_1 - \langle\langle N\rangle\rangle) - (N_2 - \langle\langle N\rangle\rangle))^2 \right\rangle \\ &= 2 \cdot \langle\langle n\rangle\rangle \cdot \langle g\rangle^2 \cdot (\frac{\sigma_n^2}{\langle n\rangle} + f)\end{aligned} \tag{9}$$

In reality, even with a larger pad size along the laser beam (6 mm), ionization electrons that reach the edge between two rows can induce charge in both rows, resulting in a correlation between the measurements of N_1 and N_2. Assuming the ionization signals collected by the two adjacent pad rows are equal, we have $\langle N_1\rangle = \langle N_2\rangle = \langle N\rangle$. As a result, the fluctuation of laser stability, $\langle(\sigma_n^2/\langle n\rangle)^2\rangle$, is effectively eliminated by measuring the charge difference received by the nearby pad rows. It follows that:

$$\begin{aligned}\frac{\sigma_n^2}{\langle n\rangle} + f &= \frac{1}{2} \cdot \frac{\left\langle (N_1 - N_2)^2 \right\rangle}{\langle g\rangle^2 \cdot \langle\langle n\rangle\rangle} \\ &= \frac{\langle\langle n\rangle\rangle}{2} \cdot \frac{\left\langle (N_1 - N_2)^2 \right\rangle}{\langle\langle N\rangle\rangle^2} \\ &= \frac{\langle\langle n\rangle\rangle}{2} \cdot \frac{\left\langle (Q_1 - Q_2)^2 \right\rangle}{\langle\langle Q\rangle\rangle^2}\end{aligned} \tag{10}$$

Therefore, the essence of determining the factor f is found in the quantification of two key deviations: the relative fluctuation in primary ionization, denoted as $\sigma_n^2/\langle n\rangle$, and the relative variance in the charge collected by adjacent pad rows, represented by $\langle(Q_1 - Q_2)^2\rangle$. As a result, our experiment will focus on accurately measuring the values of $\sigma_n^2/\langle n\rangle$ and $\langle(Q_1 - Q_2)^2\rangle$.

.

B. Experimental setup

The experimental setup is illustrated in Fig. 5(a). Firstly, it traverses a diaphragm-expander-diaphragm configuration, as detailed in Section II B. This specific arrangement reduces the laser energy to just 1% of its initial value while optimizing the beam spot diameter to 0.8 mm. Subsequently, the laser is directed into the detector through a quartz window, aligned perpendicularly to the electric field direction. The laser exits through another quartz window, and a Joulemeter monitors the laser energy.

The Triple-GEM detector, as illustrated in Fig. 5(b), has a drift length of 73 mm and is filled with T2K working gas. The detector is equipped with two quartz windows to facilitate the introduction of the laser into the chamber. Electron amplification occurs within three standard CERN GEMs [14]. The active area of each GEM is 100$\times$ 100 mm^2. The gap between the GEM foils in the transfer region is set at 1 mm, and the gap between the GEM foil and the readout pad in the induction region is 2.5 mm. This configuration is designed to maintain consistency between the experimental procedures and simulation studies, as shown in the schematic diagram in Fig. 2(b). The voltages are supplied individually by a universal multichannel power supply system (CEAN SY5527 [38]).

The readout pads, which collect electrons along the laser track, consist of 12 rows (a total of 128 pads), with each pad connected to an electronic channel, as depicted in Fig. 5(a). The pad size is 1 mm $\times$ 6 mm. The front-end electronics (FEE) are based on an ASIC named CASAGEM, which was originally designed for the GEM-TPC [39]. Each ASIC incorporates 16-channel circuits, with an equivalent noise charge (ENC) of less than 2000 for each channel. The signals from these channels pass through a CR-RC^5 circuit for filtering and shaping. The gain of the CASAGEM chip can be adjusted through four distinct settings, specifically 2 mV/fC, 4 mV/fC, 20 mV/fC, and 40 mV/fC. Analogously, the shaping time can be configured with four alternatives: 20 ns, 40 ns, 60 ns, and 80 ns. The dynamic range of the chip extends from 0 to 1000

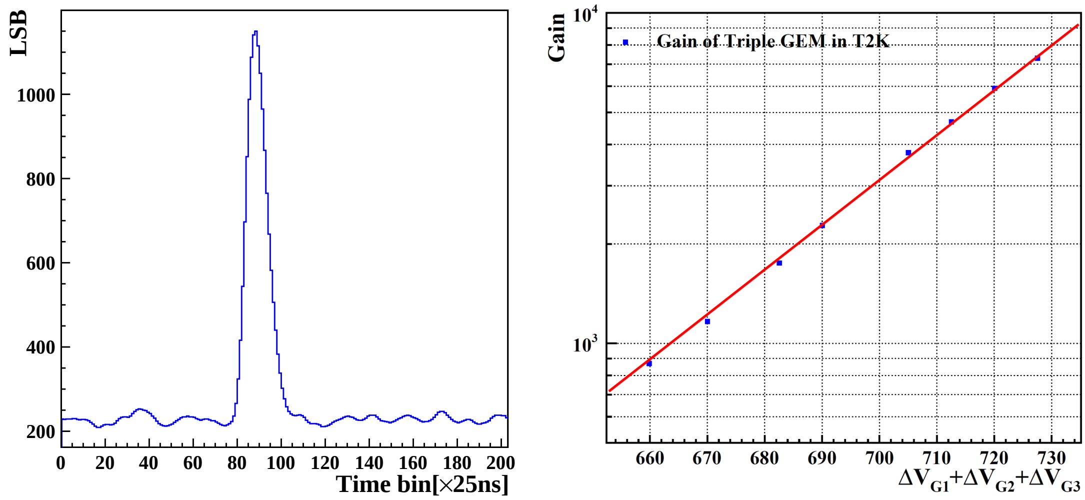

(a) (b)

Fig. 6. (a) A typical laser waveform; (b) Gain curve of the Triple-GEM detector in T2K gas, where the X-axis represents the sum of the voltages applied across the three GEM layers.

fC. Following extensive testing utilizing laser signals and a ^{55}Fe radiation source, the TPC prototype has been optimized to employ a front-end gain setting of 20 mV/fC coupled with a shaping time of 40 ns [26]. Subsequently, the analog signals are transmitted to a data acquisition (DAQ) system and digitized at 40 Million Samples Per Second (MSPS) [40].

Fig. 6(a) displays a typical laser waveform. In signal processing, the waveform's peak area, rather than its maximum value, is utilized to represent charge information, reducing the sampling frequency. The rise time is about 200 ns and the fall time is approximately 400 ns. To improve data acquisition accuracy, the calculation of the waveform area extends beyond the theoretical base width. Therefore, in our tests, we take the first 10 sampling points before the peak (250 ns) as the rise edge and the following 21 sampling points after the peak (525 ns) as the fall edge. The signal value can reach as high as 1100 Least Significant Bits (LSB), with a baseline noise ranging from 100 to 220 LSB. Furthermore, the average electronic noise level per channel is approximately 8 LSB.

IV. RESULTS

In the experimental procedure, it is essential to confirm that the DAQ and the Joulemeter monitor are operational. Subsequently, the laser is activated and an external trigger signal is provided to ensure the synchronized start of both the laser ionization signal measurement and the recording of the laser pulse energy. The experimental test lasts for 40 minutes. To maintain a direct correlation between the laser ionization signal and the laser pulse energy, the laser is turned off before the end of the data collection period, ensuring that both measurements conclude simultaneously.

The experiment initially measured the gain at various voltages across the drift, transfer, and collection regions, as illustrated in Fig. 6(b). At a total voltage differential of 660 V, the gain stands at 800, and it increases to 7500 at 730 V. For the subsequent measurement of factor f, a total voltage differential of 670 V was applied, resulting in a gain of 1040.

For the determination of the factor f, it is essential to measure the two key parameters outlined in Eq. (10), which are $\sigma_n^2/\langle n\rangle$ and $\langle (Q_1 - Q_2)^2\rangle$. It should be noted that the charge Q recorded by the electronics from the pad is directly proportional to N, and $\langle N_1\rangle = \langle N_2\rangle = \langle N\rangle$, therefore $\langle Q_1 - Q_2\rangle = 0$. Consequently, $\langle (Q_1 - Q_2)^2\rangle$ represents the standard deviation of the distribution of the difference in collected charge between adjacent pads.

The measurement of $\sigma_n^2/\langle n\rangle$ is obtained by assessing the average primary ionization resulting from the laser on the pad row. It is noteworthy that a 5.9 keV X-ray from a ^{55}Fe source can generate approximately 221 primary ionization resulting electrons, as calculated using the W-value (the average energy required per ionization) of 26.4 eV for argon in the GEM detector [41]. In our previous work, we calibrated the laser ionization using ^{55}Fe and established a power-law relationship between laser energy density and ionization density [26]. Therefore, the $\langle n\rangle$ can be estimated using the average signal charge obtained from the laser and that provided by the ^{55}Fe radiation source as follows:

$$\langle n\rangle = 221\frac{Q_{laser}}{Q_{^{55}Fe}} \tag{11}$$

Due to the high stability and repeatability of the laser, normalizing the energy of each laser incident event allows us to obtain a distribution of the average number of primary ionizations on the pad, as depicted in Fig. 7(a). The mean and standard deviation of the fitting result correspond to $\langle n\rangle$ and σ_n respectively.

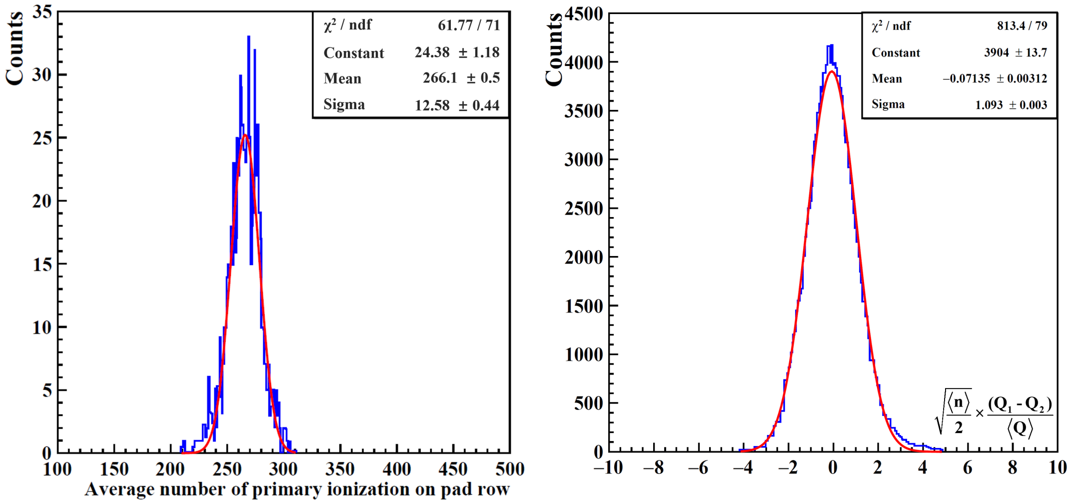

(a) (b)

Fig. 7. (a) The average primary ionization of the UV laser on the readout pad; (b) Distribution of parameter P.

Regarding the measurement of the second parameter, $\langle (Q_1 - Q_2)^2 \rangle$, a parameter P can be defined as:

$$P = \sqrt{\frac{\langle n \rangle}{2}} \cdot \frac{(Q_1 - Q_2)}{\langle Q \rangle} \tag{12}$$

the value of $\langle n \rangle$ can be obtained by each laser shot, while the other term involves a statistical calculation of the ratio between the difference in collected charge between adjacent pads and the average collected charge. By fitting the distribution of P, the standard deviation σ_P can be obtained, as shown in Fig. 7(b). Then the avalanche fluctuation factor f can be determined by:

$$\begin{aligned} f &= \frac{\langle\langle n \rangle\rangle}{2} \cdot \frac{\langle (Q_1 - Q_2)^2 \rangle}{\langle\langle Q \rangle\rangle} - \frac{{\sigma_n}^2}{\langle n \rangle} \\ &= {\sigma_P}^2 - \frac{{\sigma_n}^2}{\langle n \rangle} \\ &= 0.65 \pm 0.047 \end{aligned} \tag{13}$$

The experimental results showed an avalanche fluctuation factor f of 0.65 at a gain of approximately 1040, which is in close agreement with the simulated value of 0.66 at the same gain, thereby validating the reliability of the experimental procedure. In 2017, KEK conducted a preliminary estimation of the f using a laser, without considering the influence of laser energy fluctuations on ionization. Their findings included f values of 0.65 and 0.62 at gains of 1900 and 5800, respectively [37]. Furthermore, the notation $\langle\langle n \rangle\rangle$ was determined to be 266.1 ± 0.5. Consequently, the effective number of electrons can be estimated as $N_{eff} = 161.27 \pm 11.67$. Therefore, by adjusting the laser energy to change the value of $\langle n \rangle$ in future experiments, it may be possible to achieve a higher N_{eff}, which could subsequently enhance the position resolution of the laser in TPC applications.

V. CONCLUSION

This study utilized a Triple-GEM cascaded amplification structure to investigate the avalanche fluctuation factor f using UV laser ionization tracks. At a gain of 1040, we achieved $f = 0.65$. This method is simpler than traditional approaches, exhibits lower sensitivity to electronic noise, and offers higher repeatability. To ensure the stability of the UV laser, we conducted tests on its pointing and energy stability. The results indicated that the energy stability of the attenuated low-energy narrow-beam laser is better than 2.9%. The laser alignment stability in the X and Y dimensions was measured at 3.02 μm and 2.34 μm. Furthermore, the accurate measurement of the avalanche fluctuation factor enables the estimation of the number of effective electron N_{eff}. By adjusting the laser energy, a larger N_{eff} value can be achieved, thereby enhancing the laser's ultra-high position resolution. Consequently, the laser shows considerable potential in high-precision TPC research.

VI. ACKNOWLEDGEMENTS

The author expresses gratitude to Professor Yulan Li and Dr. Zhiyang Yuan for their insightful discussions. This research was funded by the National Key Research and Development Program (Grant No. 2016YFA0400400), the National Natural Science Foundation of China (Grant No. 11975256), and the National Natural Science Foundation of China (Grant No. 11535007).

VII. BIBLIOGRAPHY

[1] D. Attie, TPC review. Nucl. Instrum. Meth. A **598**, 89-93 (2009). doi: 10.1016/j.nima.2008.08.114

[2] H. K. Wu, X. Y. Wang, Y. M. Wang *et al.*, Fudan multi-purpose active target time projection chamber (fMeta-TPC) for photonuclear reaction experiments. Nucl. Sci. Tech. **35** 200 (2024). doi: 10.1007/s41365-024-01576-1

[3] X. G. Cao, Y. L. Chang, K. Chen *et al.*, NvDEx-100 conceptual design report. Nucl. Sci. Tech. **35**, 3 (2024). doi: 10.1007/s41365-023-01360-7

[4] K.X. Ni, Y.H. Lai, A. Abdukerim *et al.*, Searching for neutrinoless double beta decay of ^{136}Xe with PandaX-II liquid xenon detector. Chin. Phys. C **43**, 113001 (2019). doi: 10.1088/1674-1137/43/11/113001

[5] F. F. An, Y. Bai, C. H. Chen *et al.*, Precision Higgs physics at the CEPC. Chin. Phys. C **43**, 043002 (2019). doi: 10.1016/j.nima.2008.08.114

[6] H. Cheng, W.H. Chiu, Y. Fang *et al.*, The physics potential of the CEPC. Prepared for the US Snowmass community planning exercise (Snowmass 2021) (2022). doi: 10.48550/arXiv.2205.08553

[7] D. M. Asner, T. Barklow, C. Calancha *et al.*, ILC Higgs white paper. Community Summer Study 2013 : Snowmass on the Mississippi, MN, USA, 29 Jul - 6 Aug 2013. doi: 10.48550/arXiv.1310.0763

[8] M. Zhao, M.Q. Ruan, H. R. Qi *et al.*, Feasibility study of TPC at electron positron colliders at Z pole operation. J. Instrum **12** 07005 (2017). doi: 10.1088/1748-0221/12/07/P07005

[9] M. Kobayashi, R. Yonamine, T. Tomioka *et al.*, Cosmic ray tests of a GEM-based TPC prototype operated in Ar–CF4–isobutane gas mixtures. Nucl. Instrum. Meth. A **641**, 37-47 (2011). doi: 10.1016/j.nima.2011.02.042

[10] M. Kobayashi, R. Yonamine, T. Tomioka *et al.*, Addendum to "Cosmic ray tests of a GEM-based TPC prototype operated in Ar-CF4-isobutane gas mixtures". Nucl. Instrum. Meth. A **1051**, 168210 (2023). doi: doi.org/10.1016/j.nima.2023.168210

[11] D.C. Arogancia, A.M. Bacala, K. Boudjemline *et al.*, Study in a beam test of the resolution of a Micromegas TPC with standard readout pads. Nucl. Instrum. Meth. A **602**, 403-414 (2009). doi: 10.1016/j.nima.2009.01.014

[12] M. Kobayashi, R. Yonamine, T. Tomioka *et al.*, An estimation of the effective number of electrons contributing to the coordinate measurement with a TPC. Nucl. Instrum. Meth. A **562**, 136-140 (2006). doi: doi.org/10.1016/j.nima.2006.03.001

[13] W. Blum, W. Riegler, L. Rolandi, Particle detection with drift chambers, Springer Science and Business Media, (2008).

[14] F. Sauli, GEM: The gas electron multiplier (GEM): Operating principles and applications. Nucl. Instrum. Meth. A **805**, 2-24 (2016). doi: 10.1016/j.nima.2015.07.060

[15] Y. Wang, L. Zhang, A. Jung *et al.*, Simulation study of the performance of quadruple-GEM detectors. Radiat. Detect. Technol. Methods **7**, 107–116 (2023). doi: 10.1007/s41605-022-00361-1

[16] T. Alexopoulos, A.A. Altintas, M. Alviggi *et al.*, Development of large size Micromegas detector for the upgrade of the ATLAS Muon system. Nucl. Instrum. Meth. A **617**, 161-165 (2010). doi: 10.1016/j.nima.2009.06.113

[17] H. Y. Du, C.B. Du, K.Giboni *et al.*, Screener3D: a gaseous time projection chamber for ultra-low radioactive material screening. Nucl. Sci. Tech **32**, 142 (2021). doi: 10.1007/s41365-021-00983-y

[18] T. Zerguerras, B. Genolini, F. Kuger *et al.*, Understanding avalanches in a Micromegas from single-electron response measurement. Nucl. Instrum. Meth. A **772**, 76-82 (2015). doi: 10.1016/j.nima.2014.11.014

[19] Y Meng, Z Wang, Y Yao *et al.*, Dark Matter Search Results from the PandaX-4T Commissioning Run. Phys. Rev. Lett **127**, 261802 (2021). doi: 10.1103/PhysRevLett.127.261802

[20] X. Chen, C. B. Fu, J. Galan *et al.*, PandaX-III: Searching for neutrinoless double beta decay with high pressure 136Xe gas time projection chambers. Sci. China Phys. Mech. Astron. **60**(6), 061011 (2017). doi: 10.1007/s11433-017-9028-0

[21] I. COMSOL, COMSOL Multiphysics 5.5 User's Guide (2020). https://www.comsol.com/

[22] H. Schindler, Garfield++ user's guide (2023). https://garfieldpp.web.cern.ch/garfieldpp/

[23] T. Zerguerras, B. Genolini, V. Lepeltier *et al.*, Single-electron response and energy resolution of a Micromegas detector. Nucl. Instrum. Meth. A **608**, 397-402 (2009). doi: 10.1016/j.nima.2009.07.015

[24] Y. L. Zhang, H. R. Qi, B. T. Hu *et al.*, A hybrid structure gaseous detector for ion backflow suppression. Chin. Phys. C **41**(5), 056003 (2017).doi: 10.1088/1674-1137/41/5/056003

[25] H. Y. Wang, H. R. Qi, Design and study of the TPC detector module and prototype for CEPC. INT J MOD PHYS A. **34**, 1940016 (2019). doi.org/10.1142/S0217751X19400165

[26] Y. M. Cai, H. R. Qi, L. Liu *et al.*, Investigation of UV laser ionization in argon-based gas mixtures with a Triple-GEM detector. J. Instrum **15**, T02001 (2020). doi: 10.1088/1748-0221/15/02/T02001

[27] Z. Y. Yuan, H. R. Qi, Y. Chang *et al.*, Performance of TPC detector prototype integrated with UV laser tracks for the circular collider. Nucl. Instrum. Meth. A **1040**, 167241 (2022). doi: 10.1016/j.nima.2022.167241

[28] H. Y. Wang, H. R. Qi, L. Liu *et al.*, Signal and pointing accuracy of ultraviolet laser in micro-pattern gaseous detector. Acta. Phys. Sin. **68**, 022901 (2019). WLXB.0.2019-02-007

[29] M Towrie, J W Cahill, K W D Ledingham *et al.*, Detection of phenol in proportional-counter gas by two-photon ionisation spectroscopy. J. Phys. B-AT. Mol. Opt **19**, 13 (1989). doi: 10.1088/0022-3700/19/13/010

[30] S. Drysdale, K. Ledingham, C. Raine *et al.*,Detection of toluene in a proportional counter gas by resonant two photon ionisation spectroscopy. Nucl. Instrum. Meth. A **252**, 521-523 (1986). doi: 10.1016/0168-9002(86)91234-9

[31] A. Lebedev, A laser calibration system for the STAR TPC. Nucl. Instrum. Meth. A **478**, 163-165 (2002). doi: 10.1016/S0168-9002(02)01960-5

[32] J. Alme, Y. Andres, H. Appelshäuser *et al.*, The ALICE TPC, a large 3-dimensional tracking device with fast readout for ultra-high multiplicity events. Nucl. Instrum. Meth. A **622**, 316-367 (2010). doi: 10.1016/j.nima.2010.04.042

[33] H. J. Hilke, Detector calibration with lasers—A review. Nucl. Instrum. Meth. A **252**, 169-179 (1986). doi: 10.1016/0168-9002(86)91177-0

[34] Quantel Q-Smart 100 Specifications, (accessed: November 18, 2018) http://www.quantel-laser.com

[35] StarLite Entry Level Laser Power and Energy Meter http://https://www.ophiropt.com/en/f/starlite-power-meter

[36] M. Kobayashi, T.Ogawa, T.Kawaguchi *et al.*, A novel technique for the measurement of the avalanche fluctuation of gaseous detectors. Nucl. Instrum. Meth. A **845**, 236-240

(2017). doi: 10.1016/j.nima.2016.06.073

[37] M. Kobayashi, K. Yumino, T. Ogawa *et al.*, A novel technique for the measurement of the avalanche fluctuations of a GEM stack using a gating foil. Nucl. Instrum. Meth. A **1039**, 166872 (2022). doi: doi.org/10.1016/j.nima.2022.166872

[38] CEAN-SY5527 Universal Multichannel Power Supply System https://www.caen.it/products/sy5527/

[39] L. He, Z. Deng, Y. N. Liu *et al.*, Development of a multi-channel readout ASIC for a fast neutron spectrometer based on GEM-TPC. Chin. Phys. C **38**, 106101 (2014). doi: doi.org/10.1088/1674-1137/38/10/106101

[40] Y. Huang, H. Gong, J. Li *et al.*, Development of the readout system for a time projection chamber prototype. J. Instrum **14**, T01001 (2019). doi: doi.org/10.1088/1674-1137/38/10/106101

[41] H. G. Kuhn, Atomic and Molecular Radiation Physics. J. Mod. Optic **18**, 876-876 (2009). doi: doi.org/10.1080/713818393